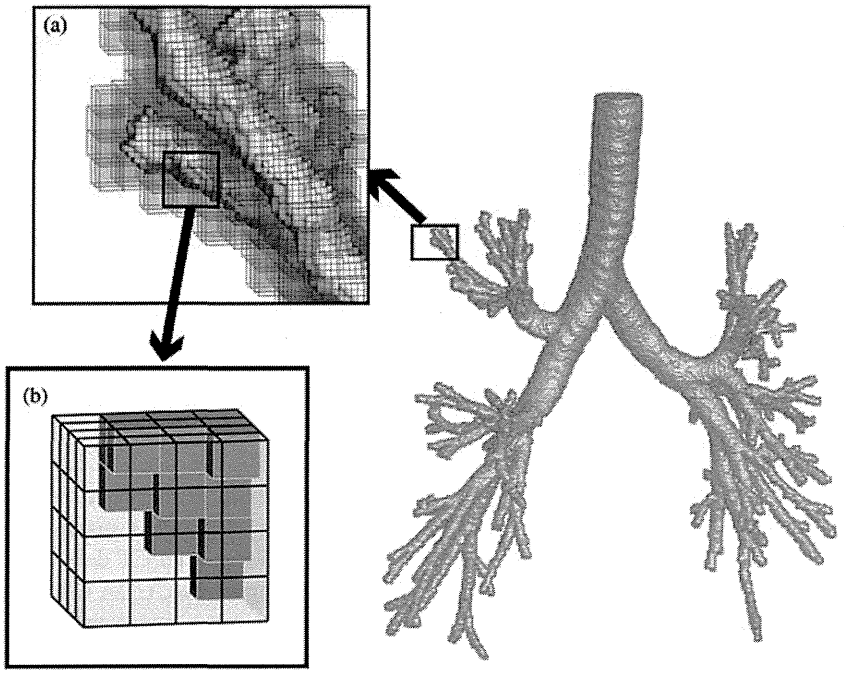

Figure 3. Schematic illustration of the adaptive meshing method: (a) the airway model is decomposed by isotropic subdomains and (b) each subdomain consists of a structured Cartesian mesh. As an example, a 4^3 size subdomain is drawn.

method: decomposing the airway into small isotropic subdomains consisting of a uniform Cartesian mesh, as shown in Figure 3. Each subdomain includes information on its connectivity to the neighbouring subdomains. Consequently, the global computational domain comprises unstructured subdomains, while the local subdomain consists of a structured Cartesian mesh, as shown in Figure 4. Although it may include unnecessary parts of the mesh in the computational domain, some recent LBM studies have used a similar form of domain decomposition (Stürmer et al. 2009; Palabos 2010) to adapt complex geometries to CPU parallel computation. In our study, decomposition is used to optimise memory access for the GPU computation. We compute each subdomain in a CUDA block, in which the block is a group of processes consisting of CUDA threads. Based on this, rather than one thread, several threads in a block co-operatively access each direction of the subdomain connectivity information at once via coalesced memory access, which accelerates the calculation.

Note that the size of the subdomains should be determined carefully because the ratio of the airway mesh to the entire mesh is highly dependent on this, and it also changes the appropriate number of CUDA threads for the computation in a subdomain. To determine the optimal subdomain size, we evaluated the filling ratio, two performance indices and memory usage. The filling ratio compares the number of airway (fluid) mesh components (N_a) to the total number of mesh components (N_g), including the unnecessary mesh components, and it is defined by

$$\text{Filling ratio} = \frac{N_a}{N_g}. \tag{10}$$

The two GFLOPS performance indices used are

$$\text{Real performance (GFLOPS)} = \frac{O \times N_g}{T \times S} \frac{1}{1024^3}, \tag{11}$$

$$\text{Effective performance (GFLOPS)} = \frac{O \times N_a}{T \times S} \frac{1}{1024^3}. \tag{12}$$

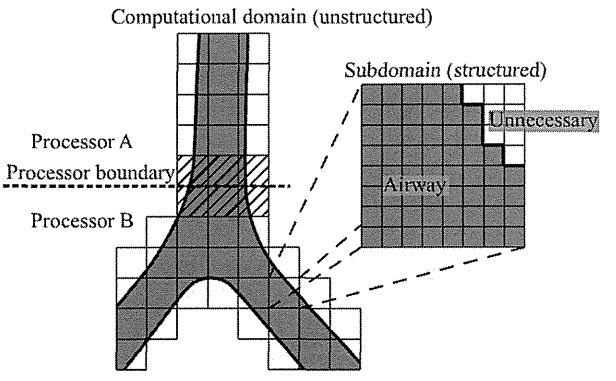

Figure 4. Schematic illustration of mesh hierarchy. The area in grey represents airway mesh, and the area in white is unnecessary mesh. Processor boundary in multi-GPU computation is also shown. Subdomains near processor boundary are indicated by the shaded area.

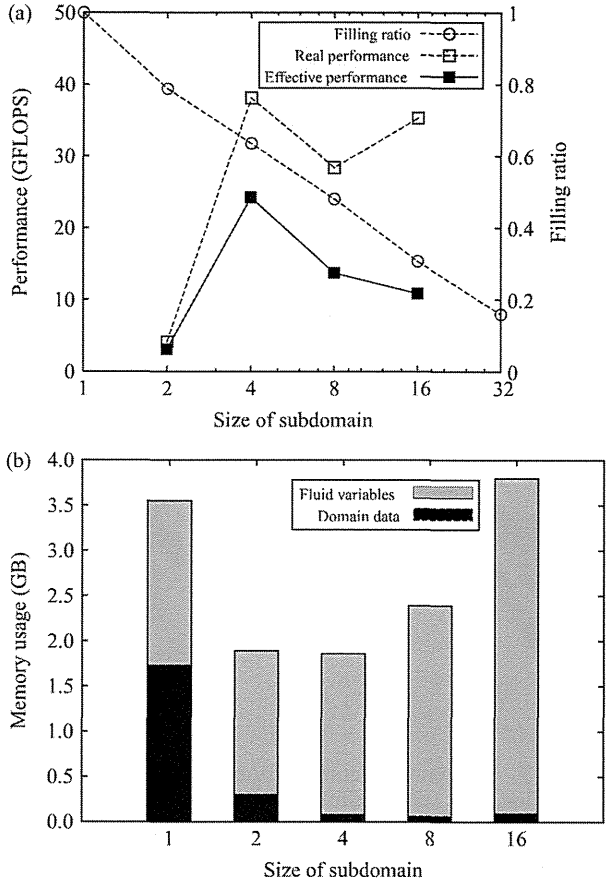

Figure 5. Results of the tests to determine the optimal subdomain size: (a) the filling ratio and performance indices and (b) memory usage.

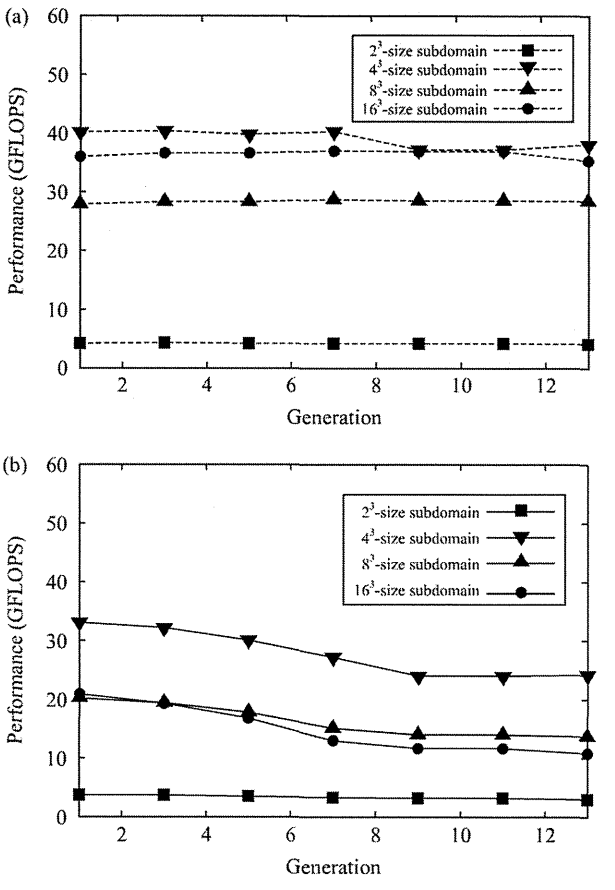

Figure 6. Effects of geometry complexity: (a) real performance and (b) effective performance.

In these, O is the number of floating-point operations ($O = 229$ in our D3Q19 LBGK model), T is the computational time and S is the number of computational steps. From the definition, the real performance represents the effort expended for the entire domain and the effective performance is the effort expended for the airway domain.

Figure 5(a) shows the results for the computation of the airway model in Figure 2 for subdomain sizes ranging from 1^3 to 32^3, performed on an nVIDIA Tesla C1060 GPU. As a large subdomain includes many unnecessary mesh components, the filling ratio decreases as the subdomain size increases. The real performance of a 2^3 size subdomain is the poorest, as only eight threads, which is smaller than the warp size, are used to compute one subdomain according to our CUDA block usage. The term 'warp' refers to the group of threads processed at one time; one warp consists of 32 threads for CUDA version 3.1, whereas 64 threads are used in a 4^3 size subdomain computation and 256 threads are used in 8^3 size and 16^3 size subdomain computations. The real performance of 4^3 size to 16^3 size subdomains ranges between 30 and 40 GFLOPS. However, the filling ratio decreases for the larger subdomains, and the effective performance is the highest for the 4^3 size subdomain. The memory usage for stored fluid variables and domain data is shown in Figure 5(b). As the subdomain size increases, the memory used to store fluid variables increases due to the increase in unnecessary mesh components. The subdomain connectivity information is stored for the entire mesh in the case of 1^3 size subdomains; thus, the memory usage for the domain data is the greatest. The minimum memory usage occurs using 4^3 size subdomains. To check whether the optimum subdomain size is affected by the complexity of geometry, we compared different geometries that were constructed by pruning airway branches from the original 13-generation airway model. We constructed 1- to 13-generation airway models, in which the complexity increases with the number of generations. The result is shown in Figure 6. The effective performance decreases as the geometry becomes more complex, owing to the decrease in the filling ratio, whereas the real performance is affected less by the geometry complexity for all subdomain sizes. In conclusion, GPU computations using 4^3 size subdomains have the greatest effective

performance for any airway model. An airway model covered by 4^3 size subdomains, consisting of 11,265,536 mesh components with 176,024 subdomains, is shown in Figure 3.

4. Comparison of the performance of multi-GPU and multi-CPU computations

We adapted the patient-specific model to multi-GPU computation using a message passing interface (MPI) library. As all of the fluid variables are stored in the GPU device memory and updated at every time step, additional data transfer protocols are needed compared with multi-CPU computation. First, the data in the device memory are transferred to the host computer memory through a PCI Express bus. After the data transfer, the data are exchanged among cluster nodes through InfiniBand using the MPI library. Finally, the exchanged data are copied from the host memory to the device memory through the PCI Express bus. As the GPU has the ability to compute much faster than the CPU and additional data transfer protocols are needed for GPU computation, the data transfers easily become bottlenecks in terms of the overall computational time. To reduce these bottlenecks, the subdomains near the processor boundary, as shown in Figure 4, are computed first, then the data transfers and computation of non-processor boundary subdomains are processed simultaneously. As the mesh components are clustered into subdomains, domain decomposition for multi-GPU computation is accomplished easily. For domain decomposition, we primarily consider the load balance among processors. Therefore, in our computation, the subdomains are grouped from the trachea to the peripheral airways, controlling the numbers of grouped subdomains so that they are nearly equal. For example, the domain decomposition for eight-processor computation is shown in Figure 7.

We compared the performance of entirely multi-GPU computation with that of multi-CPU computation. The tests were performed on TSUBAME 1.2, a supercomputer system at the Tokyo Institute of Technology, using the airway model constructed in Section 3. The system has 657 nodes of AMD Opteron CPUs (total 10,512 cores), of which 170 nodes are connected to nVIDIA Tesla S1070 GPU devices. All of the nodes are connected with InfiniBand. The effective performances of multi-GPU and multi-CPU computations are shown in Figure 8(a). We found that about 800 CPU cores must be recruited for performance that equals eight-GPU computations. The scalability of the GPU computation peaks at eight GPUs, while the CPU computation peaks at 32 CPU cores. This indicates that the time required for data transfer cannot fully overlap with other processes in computations involving more than 16 GPUs. Taking the opposite view,

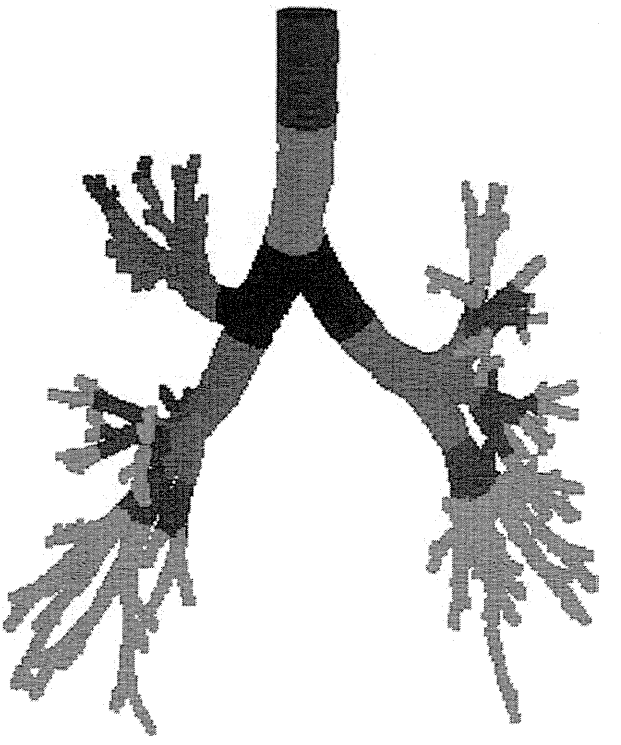

Figure 7. Domain decomposition for eight-processor computation. The subdomains shown in the same colour were computed using the same processor.

eight GPUs are sufficient to compute pulmonary airflow consisting of 12 million mesh components.

The same computation was performed on a small cluster involving eight personal computers, each mounting the latest quad-core CPU, Intel Core i7-930, and the latest GPU, nVIDIA GeForce GTX 480. GeForce GTX 480 is connected to the GDDR5 device memory, which has a bandwidth of 177.4 GB/s, whereas Core i7-930 is connected to triple-channel DDR3-1066 host memory, which has a bandwidth of 25.6 GB/s. All computers are connected using a 40-Gbps QDR InfiniBand. This cluster costed less than $30,000 in the spring of 2010 and occupies a footprint of 0.7 m^3, so it could be installed in medical offices. The result of the benchmark test is shown in Figure 8(b), which shows that high-performance computation can also be performed on personal-use GPUs. Figure 8(b) plots the effective performance for GPU computation and real performance for CPU computation, assuming that it may not be necessary to apply the developed adaptive meshing method, which includes unnecessary mesh components, in the CPU computation. Nonetheless, comparing the effective performance of GPUs with the real performance of CPUs, the result shows that 170 CPU cores, which are nearly equal to 42 quad-core CPUs, are needed to attain the performance of eight GPUs, even if the CPU computation could attain scalability. As the LBM handles 23 variables in each lattice component, particle distributions moving

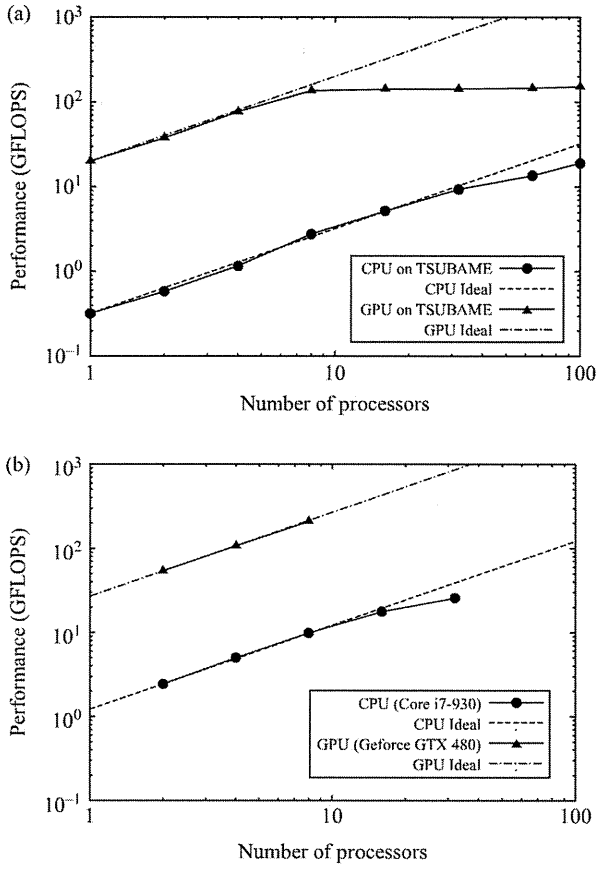

Figure 8. Benchmark test: multi-CPU vs. multi-GPU: (a) benchmark on TSUBAME 1.2 and (b) benchmark on a small cluster system.

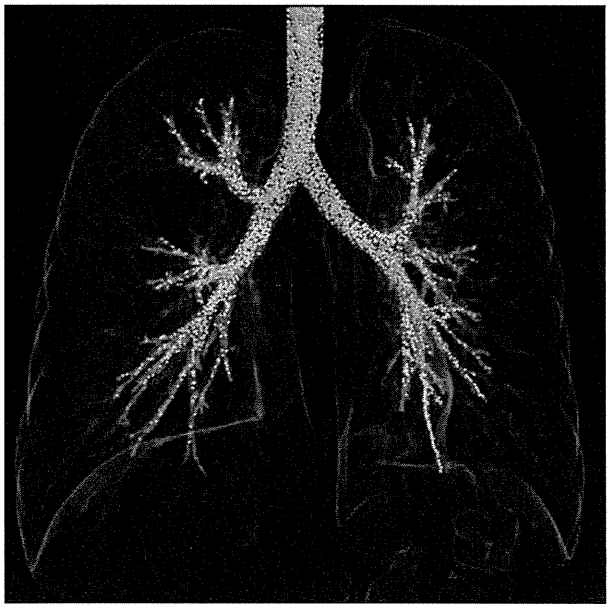

Figure 9. Particles are tracked along airflow streamlines, and the data are overlapped with volume rendered lung data from the same subject.

in 19 directions, three-dimensional velocity and density, an advantage exists on using GPUs connected to a very wide-bandwidth device memory. A simulation of inspiratory airflow is shown in Figure 9, in which particles are tracked along airflow streamlines, and the data are overlapped with a volume rendered lung data generated from the same subject. Freitas and Schröder (2008) reported a large-scale pulmonary airflow simulation using the LBM on a supercomputer system in the Jülich supercomputing centre. They used a mesh with 12 million components for the simulation, almost identical to the number we used; such a computation can be performed on a small GPU cluster using our LBM solver.

5. Conclusions

We proposed a novel approach for the patient-specific modelling of pulmonary airflow. The computational time is a major issue in the application of patient-specific models to medical practice. To overcome this problem, we developed an LBM flow solver for the use on GPU clusters. The LBM is a fully explicit solver free of the convergence problem of pressure Poisson equations encountered in semi-implicit methods. Moreover, high-performance computation can be achieved on a GPU with a wide-bandwidth device memory because the performance of the LBM depends strongly on the memory access speed. As adequate memory usage is essential for GPU computation, we also developed an adaptive meshing method for the complex pulmonary airway model. In this method, the airway model is covered by small isotropic subdomains consisting of a Cartesian mesh. The computational mesh can be generated directly from CT data, as the data consist of voxels aligned in Cartesian coordinates. We demonstrated that 4^3 size subdomains perform the best for patient-specific models of up to 13-generation airways. We confirmed that the proposed model with 12 million mesh components has scalability up to eight GPUs on TSUBAME 1.2, which are sufficient for simulating this model, while more than 800 CPU cores are needed to obtain the same results, even if the CPU could retain its scalability. The computation can also be performed on a small personal-use GPU cluster within a reasonable price and footprint. Eighty minutes is required to simulate the airflow for 1 s, or 5 h to obtain the results for one 4-s cycle of respiration, which would be reasonable for practical use in clinical diagnosis.

We will be able to analyse gas exchange phenomena or nanoparticle deposition in the airways simply by coupling advection–diffusion equations or the Lagrangian tracking of particles with this method. Such an analysis will provide useful supporting information for diagnosis and treatment. Although the GPU computation shows potential for CFD problems, an application to complex geometry problems has not been fully developed. This is a particularly crucial

issue in biomedical engineering because almost all organs have complex geometries. Our method can be applied to any complex geometry problem, such as the patient-specific modelling of blood flow. We hope that this method will lead to the efficient use of patient-specific models in a variety of medical applications.

References

Balásházy I, Hofmann W. 1993a. Particle deposition in airway bifurcations – I. Inspiratory flow. J Aerosol Sci. 24(6): 745–772.

Balásházy I, Hofmann W. 1993b. Particle deposition in airway bifurcations – II. Expiratory flow. J Aerosol Sci. 24(6): 773–786.

Comeford A, Förster C, Wall WA. 2010. Structured tree impedance outflow boundary conditions for 3D lung simulations. J Biomech Eng. 132:081002.

Corrigan A, Camelli FF, Löhner R, Wallin J. 2010. Running unstructured grid-based CFD solvers on modern graphics hardware. Int J Numer Meth Fluids. 66(2):221–229.

CUDA C best practices guide. [cited 2010 Sep 20]. Available from: http://developer.nvidia.com/

CUDA C programming guide. [cited 2010 Sep 20]. Available from: http://developer.nvidia.com/

De Backer JW, Vos WG, Devolder A, Verhulst SL, Germonpré P, Wuyts FL, Parizel PM, De Backer W. 2008. Computational fluid dynamics can detect changes in airway resistance in asthmatics after acute bronchodilation. J Biomech. 41: 106–113.

De Backer JW, Vos WG, Vinchurkar SC, Claes R, Drollmann A, Wulfrank D, Parizel PM, Germonpré P, De Backer W. 2010. Validation of computational fluid dynamics in CT-based airway models with SPECT/CT. Radiology. 257:854–862.

Freitas RK, Schröder W. 2008. Numerical investigation of the three-dimensional flow in a human lung model. J Biomech. 41:2446–2457.

Gemci T, Ponyavin V, Chen Y, Chen H, Collins R. 2008. Computational model of airflow in upper 17 generations of human respiratory tract. J Biomech. 41:2047–2054.

Kuznik F, Obrecht C, Rusaouen G, Roux J. 2010. LBM based flow simulation using GPU computing processor. Comput Math Appl. 59:2380–2392.

Lin CL, Tawhai MH, McLennan G, Hoffman EA. 2007. Characteristics of the turbulent laryngeal jet and its effect on airflow in the human intra-thoracic airways. Respir Physiol Neurobiol. 157:295–309.

Nowak N, Kakade PP, Annapragada AV. 2003. Computational fluid dynamics simulation of airflow and aerosol deposition in human lungs. Ann Biomed Eng. 31:374–390.

Palabos., [cited 2010 Sep 20]. Available from: http://www.lbmethod.org/palabos/

Qian YH, D'Humières D, Lallemand P. 1992. Lattice BGK models for Navier-Stokes equation. Europhys Lett. 17(6): 479–484.

Riegel E, Indinger T, Adams NA. 2009. Implementation of a lattice-Boltzmann method for numerical mechanics using the nVIDIA CUDA technology. CSRD. 23:241–247.

Rochefort L, Vial L, Fodil R, Mâtre X, Louis B, Isabey D, Caillibotte G, Thiriet M, Bittoun J, Durand E, et al. 2007. *In vitro* validation of computational fluid dynamic simulation in human proximal airways with hyperpolarized ^{3}He magnetic resonance phase-contrast velocimetry. J Appl Physiol. 102:2012–2023.

Stürmer M, Götz J, Richter G, Dörfler A, Rüde U. 2009. Fluid flow simulation on the cell broadband engine using the lattice Boltzmann method. Comput Math Appl. 58:1062–1070.

Thibault JC, Senocak I. 2010. Accelerating incompressible flow computations with a Pthreads-CUDA implementation on small-footprint multi-GPU platforms. J. Supercomput (Published online).

Tölke J. 2010. Implementation of a lattice Boltzmann kernel using the compute unified device architecture developed by nVIDIA. Comput Visual Sci. 13:22–39.

van Ertbruggen C, Hirsch C, Paiva M. 2005. Anatomically based three-dimensional model of airways to simulate flow and particle transport using computational fluid dynamics. J Appl Physiol. 98:970–980.

Yang XL, Liu Y, Luo HY. 2006. Respiratory flow in obstructed airways. J Biomech. 39:2743–2751.

Yin Y, Choi J, Hoffman EA, Tawhai MH, Lin CL. 2010. Simulation of pulmonary air flow with a subject-specific boundary condition. J Biomech. 43:2159–2163.

Zhang Z, Kleinstreuer C, Donohue JF, Kim CS. 2005. Comparison of micro- and nano-size particle depositions in a human upper airway model. J Aerosol Sci. 36:211–233.

Zhao Y. 2008. Lattice Boltzmann based PDE solver on the GPU. Visual Comput. 24:323–333.

J Mol Model (2011) 17:2773–2780
DOI 10.1007/s00894-010-0946-7

ORIGINAL PAPER

Adsorption mechanism of single guanine and thymine on single-walled carbon nanotubes

Muthusivarajan Rajarajeswari · Kombiah Iyakutti · Yoshiyuki Kawazoe

Received: 2 November 2010 / Accepted: 27 December 2010 / Published online: 29 January 2011

Abstract Bio-nano hybrids introduce magnificent applications of nanomaterials to various fields. The choice of carbon nanotube as well as sequence selection of the nucleic acid bases play a crucial role in shaping DNA–carbon nanotube hybrids. To come up with a clear vision for the choice of carbon nanotube and nucleic acid bases to create bio-nano hybrids, we studied the adsorption mechanism of the nucleic acid bases guanine and thymine on four different types of nanotubes based on density functional theory. Nucleic acid bases exhibit differential binding strengths according to their structural geometry, inter-molecular distances, the carbon nanotube diameter, and charge transfer. The π–π interaction mechanism between the adsorbent and adsorbate is discussed in terms of charge density profile and electronic band structure analysis.

Keywords Carbon nanotube · Nucleic acid base · π–π stacking interaction · Density functional theory

Introduction

The study of the noncovalent interactions of biological molecules with single-walled carbon nanotubes (SWCNT) has emerged as a separate field in nanotechnology. Functionalization of CNT with biomolecules leads to many potential applications in medicinal biology as well as in solid state nano electronics. Carbon nanotubes are being explored as one of the most promising transfection vectors for drug and gene delivery, due to their large surface area, stability, flexibility and biocompatibility. Hybrids of SWCNT-ribonucleic acid (RNA) polymer formed through nonspecific binding are translocated into MCF7 breast cancer cells with radioscope labeling [1]. SWNTs have the ability to penetrate mammalian cells as intracellular protein transporters with noncovalently bound protein cargo [2]. An electronic biosensor for detecting antibodies associated with human autoimmune diseases has been developed through the nonspecific binding of proteins on carbon nanotubes [3]. Carbon nanotubes decorated with peptide is used in a field effect transistor (FET)-based chemical sensor to detect specific targets using peptide recognition elements [4].

Deoxyribonucleic acid (DNA) overstated its role not only in biology, but also in nanotechnology. Integration of carbon nanotubes with the genetic material DNA opens up several possible applications of CNT in the field of bio-nanotechnology. Over a decade of research has now contributed to our understanding of the interactions in DNA–CNT hybrids. Nonspecific interaction of CNTs with DNA helps the dispersion and separation of CNTs in aqueous and non-aqueous solution, while leaving the unique physical and electronic properties of CNTs unchanged. The helical wrapping of poly(T) on a carbon nanotube (10, 0) converts CNT into a water soluble object and helps to sort the carbon nanotubes with respect to their electronic properties [5]. Self-assembly of the sequence $d(GT)_n$ around individual nanotubes enables nanotube separation using ion exchange liquid chromatography [6, 7]. In the study of a

M. Rajarajeswari · K. Iyakutti (✉)
School of Physics, Madurai Kamaraj University,
Madurai, Tamil Nadu 625 021, India
e-mail: iyakutti@yahoo.co.in

Y. Kawazoe
Institute for Materials Research, Tohoku University,
Sendai 980-8577, Japan

molecular dynamics simulation of a self-assembly of random sequence ssDNA on CNT, achiral loops and disordered kinked structures are observed due to the flexibility of ssDNA [8]. Also, the helical wrapping of poly (GT) on CNT [6, 7] is claimed to be structurally unstable, and the oligonucleotide does not prefer to be adsorbed onto CNTs as a dimer. "Ultrasoft" DNA sequencing have been performed by detecting the variation in the current through a CNT when different DNA base pairs are in contact with the CNT [9]; the individual nucleosides adsorbed on the CNT are also identified with the applied external gate voltage [10]. These results shows that the adsorption mechanism of nucleic acid bases on CNT varies with respect to each nucleic acid base. Depending on the length and the sequence of nucleic acid bases in the DNA, a large molecular library is available from which to produce a number of DNA–CNT hybrids, leading to a wider range of magnificent applications. In its simplest form, individual nucleic acid bases can interact with CNTs singly or in multiples (poly). Interactions of isolated nucleic acid bases with CNTs have been studied using density functional theory (DFT) with different functionals [11, 12], and with Raman spectroscopic technique [13]. Das et al. [14] investigated the binding of nucleobases with CNT by means of Hartree-Fock (HF) theory and isothermal calorimetry experiments. Atomistic molecular dynamics (MD) simulations were performed to study the binding of nucleotide monophosphates with (6, 0) SWCNTs in aqueous solution [15]. From previous reports, it is clear that generally binding of DNA to CNT depends generally on the nucleotide sequence and the nanotube diameter [16].

In earlier reports, binding energies of all five nucleic acid bases with a carbon nanotube is calculated using different density functional codes [11–17]. Interaction strength varies in the order G>A>T>C>U [11, 13, 14]. Self-stacking interactions of nucleobases compete with the cross-stacking interaction strength of nucleobases with CNT [18]. Thus, the interaction strength of nucleobases with CNT should be able to overcome the self-stacking interactions. Using ion exchange chromatography technique, Zheng et al. [5–7] proved the ability of poly (T) and poly (GT) to disperse CNTs in aqueous solution. Of the four nucleobases, from the relative binding energies of self-stacking nucleobases and cross-stacking on CNT, Wang [18] proved that thymine can disperse CNT in aqueous solution better than adenine and cytosine. Consequently, the nucleic acid bases thymine and guanine have gained importance in the dispersion of CNTs. Like the differential adsorption strength of nucleic acid bases, different chiralities of CNT also play a significant role in the binding strength of CNT–nucleic acid base hybrids. Earlier reports concentrated on finding the variation in binding energies of different nucleic acid bases with a CNT. Some reports presented electronic band structure analysis and iso surface charge density plots [11, 17], and examined the interaction between them. However, we choose to investigate the role of the curvature and chirality of the CNT in the formation of DNA–CNT hybrid. In our study, to expand our knowledge of the interaction between the nucleic acid bases thymine and guanine and CNTs of different chiralities, with the help of standard density functional code, we present the role of geometry, adsorption mechanism, charge transfer, electronic band structure analysis and charge density analysis.

Computational details

Calculations were carried out using DFT with a plane wave basis set as implemented in the Vienna ab-initio simulation package (VASP) [19, 20]. The projected augmented-wave method (PAW) is used to describe the interaction between ions and electrons [21]. The PAW method has two advantages over ultrasoft pseudo potentials (USPP). It provides all-electron wave functions for valence electrons and shows a better convergence behavior than USPP [21]. DFT is used to describe the ground state properties of many-body systems. Exchange correlation energy can be evaluated with the help of local density approximation (LDA) [22] or with generalized gradient approximation (GGA) [23]. Non-covalent interaction between the two systems is the result of van der Waals, hydrogen bonding, ion-pairing, cation–π and π–π interactions. It is well known that neither LDA nor GGA can describe weakly bound systems perfectly. A considerable effect of exchange correlation energy functionals in the binding energy was noted with DFT techniques. Generally, LDA overestimates the interaction energy of weakly bound systems and GGA underestimates it. Here, our aim was to study non-covalent interactions between DNA–CNT hybrids, thus we had to be very precise in choosing an exchange correlation functional with which to determine accurate interaction energies and structural properties. DFT-LDA calculations underestimate dispersion energy at large distances but can reproduce the empirical potential for graphitic structures successfully [24]. Studies on self-stacking of benzene and cross stacking of benzene on graphene sheet within GGA have shown almost no binding energy [25]. However, the interlayer distance for adenine adsorption on graphene sheet reported using the DFT-LDA technique is very close to the experimental result [26]. Most recently, Lim and Park [27] have investigated the noncovalent adsorption of aromatic molecules on CNT with the help of LDA, GGA and hybrid functionals. It was found that DFT-LDA and M06 hybrid functionals produce almost equal binding energy, and that GGA fails to predict the noncovalent interaction. With this

previous literature support, we decided to follow the LDA approach to investigate the exchange correlation energy of our weakly bound systems.

For k-points sampling of the brillouin zone, a 1×1×4 Monkhorst-Pack grid [28] is used with a spacing of 0.025 $Å^{-1}$. For the electronic band structure calculations, 41 irreducible k-points are considered along the *z*-axis direction. Cutoff energy for the plane wave basis set of the valence electron was fixed as 500 eV throughout the calculations. Residual minimization / direct inversion in the iterative subspace method (RMM–DIIS) is used for wave function optimization. Geometry optimization was carried out until the magnitude of the forces acting on all atoms was smaller than 0.0005 eV/Å. The CNTs zigzag (5, 0), (10, 0), armchair (5, 5) and chiral (5, 2) were used in this study. The number of unit cells of CNT is limited by the height of the nucleic acid bases. In all four cases, approximately 20 Å distance is kept between adjacent tubes to avoid interactions between them. Thymine and guanine are nucleic acid bases found in the genetic material DNA. Thymine is a pyrimidine nucleobase, having one hexagon ring with two nitrogen atoms. Guanine is a derivative of purine consisting of a fused pyrimidine-imidazole system with conjugated double bonds. Initially, the hexagon of the nucleic acid base is kept head-to-head with the hexagon of the carbon nanotube. The plane of the nucleic acid base is parallel with the nanotube *z*-axis direction. Atoms are allowed to relax freely in all directions, to determine the possible adsorption positions of nucleic acid bases on the CNT surface.

Results and discussion

Geometry and energetics of adsorption of guanine and thymine on SWCNTs

Prediction of accurate interaction energy of the adsorbate with the adsorbent involves description of intermolecular parameters such as the orientation of the adsorbate, and inter-molecular distances between the adsorbent and adsorbate. These parameters play a significant role, especially in the case of non-covalent interactions. During geometry optimization, the initial orientation of nucleic acid bases on CNTs was altered to attain the minimum energy configuration, but the nucleic acid bases are still parallel to the nanotube surface. The distance between the CNT and each nucleic acid base is measured from the center of the hexagonal ring of the adsorbate to the nanotube surface. Binding energies, equilibrium distances and charge transfer from the nucleic acid bases to the CNT are presented in Table 1. There is no chemical bond formation between the systems and the binding energies confirm that the process is physisorption. The oxygen and nitrogen atoms of nucleic acid bases have lone pairs of electrons and, due to the sp^2 hybridization of carbon atoms in the CNT, each carbon atom possesses one delocalized p electron. These π electrons lead to physisorption of the nucleic acid bases on the CNT.

Intermolecular distances between the CNT and the nucleic acid bases guanine and thymine vary between 2.46 and 3.26 Å. These values are comparable to those reported in previous studies [13, 17]. Among the four nanotubes, thymine is adsorbed close to CNT (10, 0) at a distance of 2.46 Å, which is less than the characteristic π–π stacking distance. Intermolecular separation of adenine on graphite surface is reported as 3.1 Å within LDA, and AFM studies give the same value [26]. As reported by Stepanian et al. [13], the difference between intermolecular distances estimated using second-order Moller-Plesset perturbation theory (MP2) and DFT is about 0.02 Å. Thus, the calculated intermolecular separation of a non-covalently bound system using DFT-LDA is comparable with the results obtained from experiments and MP2 methods. Adsorption of nucleic acid bases on CNT resembles AB stacking between graphene layers. The orientation of nucleic acid bases on the surface of the CNT differs with

Table 1 Binding energies, charge transfer, equilibrium distances for the adsorption of guanine and thymine on carbon nanotubes (CNTs), and diameter of CNTs

System	Binding energy (E_b, eV)	Charge transfer from nucleic acid base (q, e)	Distance (d, Å)	Diameter (d_t, Å)
CNT (5, 0)+Guanine	0.41	0.094	3.07	3.96
CNT (5, 2)+Guanine	0.36	0.009	3.05	4.95
CNT (5, 5)+Guanine	0.38	0.001	2.98	6.87
CNT (10, 0)+Guanine	0.39	0.008	3.06	7.94
CNT (5, 0)+Thymine	0.20	0.026	3.26	3.96
CNT (5, 2)+Thymine	0.26	0.005	2.95	4.95
CNT (5, 5)+Thymine	0.30	0.009	2.97	6.87
CNT (10, 0)+Thymine	0.20	0.014	2.46	7.94

CNT chirality so as to attain the minimal energy configuration.

The binding energy of guanine with a narrow nanotube (5, 0) is 0.41 eV, and the tube becomes compressed in the direction of the adsorbate. The radius of the tube is reduced to 1.87Å in the strained direction (Fig. 1a,e). In studies of interaction between nanotubes and biomolecules, to reduce the computational expense, fragmented CNTs have been used [13, 18]. Fragmenting material such as high-curvature CNT may not give reliable results. Wang [18] examined the adsorption of DNA nucleic acid bases with fragments derived from CNTs (5, 5) and (10, 0). The CNT fragments were frozen with saturated H atoms, thus limiting the interaction of the CNT with the nucleic acid base. This will surely affect the binding energy of the nucleic acid base, whereas we have taken the fully relaxed CNT and allowed all the atoms to move freely in all three directions. Wang [18] reported more than one stable configuration of nucleic acid base on CNT, with a binding energy for guanine varying from 0.32 to 0.44 eV for CNT (5, 5) and from 0.22 to 0.34 eV for CNT (10, 0) without basis set superposition error (BSSE) correction. In another study using MP2 level theory, binding energies of guanine with CNT (5, 5) in the order of 0.36 to 0.88 eV were reported [13]. The curvature-free surface of graphene facilitates the adsorption of planar molecules compared to narrow nanotubes [29]. Except in the case of CNT (5, 0), the binding energy of guanine increases with increasing CNT diameter (Table 1).

Optimized structures of CNT+thymine complexes are presented in Fig. 2. The parallel orientation of thymine helps the interaction between the π orbitals of CNT and thymine. In the adsorption of thymine on CNT (5, 0), the upper half of thymine gets very close to the CNT (Fig. 2e). The lone pair of electrons present in the nitrogen and oxygen atoms caused a tilt in the parallel orientation of thymine on the CNT surface but still the thymine remains planar without pyramidalization. Due to π electron cloud interactions between the CNT and thymine, the CNT becomes distorted in the direction of the adsorbate, like in the CNT (5, 0)+G complex. Here the radius of the (5, 0) tube shrinks to 1.92Å. In the other three cases , the adsorbate does not lead to any change in the CNT structure. Wang [18] analyzed the ability of thymine to disperse SWCNTs by investigating the adsorption of nucleic acid bases on CNT in the gas and aqueous phases. The reported binding energies in the gas phase using MPWBIK functional are in the range of 0.11 to 0.29 eV for the different orientations of thymine on CNT (5, 5), and these values agree well with our results (Table 1).

CNT (10, 0) is a wide tube, with a lesser curvature effect compared to the other nanotubes considered in this study. The binding energy of thymine with CNT (10, 0) is 0.20 eV. In a study of the interaction of thymine/thymine radicals with CNT (10, 0) [17], binding energies in the order of 0.22 to 0.31 eV are reported, which is comparable with our results. However, the binding energy of thymine with CNT (10, 0) is expected to be higher than the other narrow nanotubes. In the optimized structure of CNT (10, 0)+T (Fig. 2d), thymine is positioned at a distance of 2.46Å. This is the shortest intermolecular distance of all the nanotubes tested here. Two CO and NH groups of thymine are tilted towards the CNT. The intermolecular distance between the adsorbent and adsorbate plays a key role in the π-stacking interaction. The π–π repulsive interaction between the adsorbent and adsorbate causes the system to have a certain distance of separation called the characteristic distance of π-stacking, so as to minimize the exchange repulsive interaction between them. Electronegative oxygen and nitrogen atoms present in thymine are thus dragged towards the CNT; this increases the repulsive interaction between the thymine and the CNT and results a considerable reduction in the binding energy.

Generally, π–π interaction energy is the result of electrostatic, induction, charge transfer, dispersion and repulsive energies between the adsorbent and adsorbate [30]. DFT fails to describe the dispersion interaction of

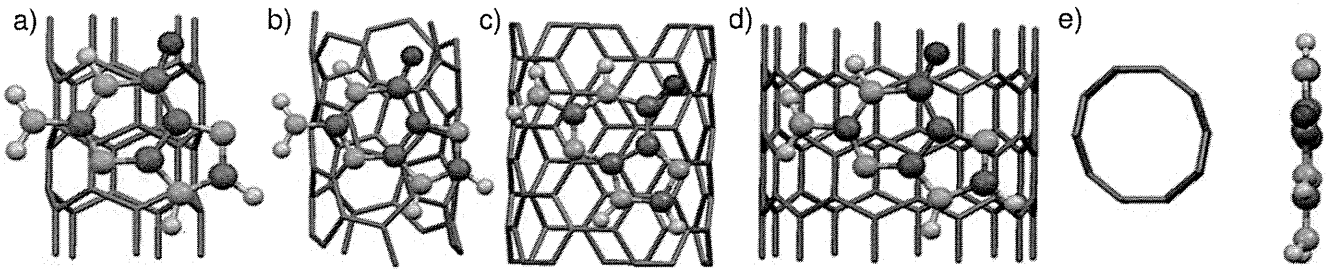

Fig. 1a–e Optimized configurations of guanine adsorbed on carbon nanotubes (CNTs). **a** CNT (5, 0)+G; **b** CNT (5, 2)+G; **c** CNT (5, 5)+G; **d** CNT (10, 0)+G; **e** CNT (5, 0)+G

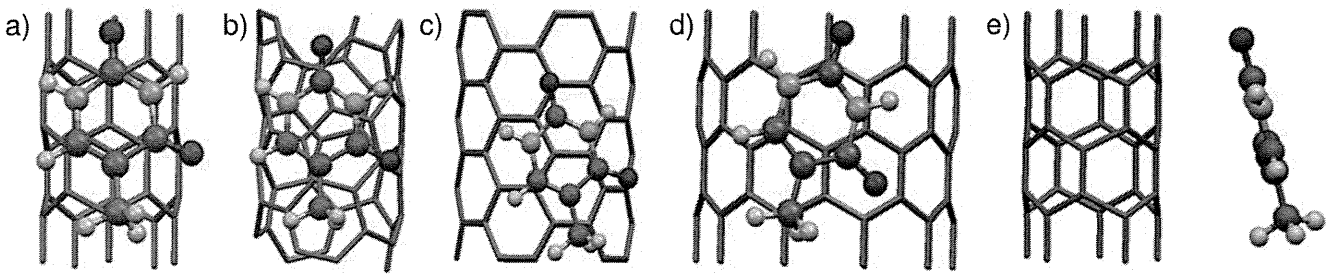

Fig. 2a–e Optimized configurations of thymine adsorbed on CNTs. **a** CNT (5, 0)+T; **b** CNT (5, 2)+T; **c** CNT (5, 5)+T; **d** CNT (10, 0)+T; **e** CNT (5, 0)+T

noncovalent systems at very large distances. Calculating the interaction energy perturbatively using symmetry-adapted perturbation theory (SAPT) [31] can describe such intermolecular interactions, including dispersion energy. SAPT interaction energy is expressed as the sum of electrostatic, exchange, induction, exchange-induction, dispersion and exchange-dispersion components. It is a very successful technique for molecules of ten atoms or fewer but is not suitable for large systems. In our case, the intermolecular separation between CNT and nucleic acid base varies between 2.46 and 3.26Å. With this intermolecular separation, DFT-LDA can determine the interaction energy of the noncovalent system successfully [24]. Here, the binding energy results from electrostatic, induction, charge transfer and repulsive interactions.

Charge transfer and charge density analysis

Bader charge density analysis [32] was performed to determine the total charge associated with each atom and to investigate possible charge transformation between the two entities. Although there is no direct chemical bonding between the adsorbate and CNT, we can expect a fractional charge transfer between them due to the π electrons and lone pair of electrons. In a similar situation, Stepanian et al. [13] observed a downshift of G-band frequency in the Raman spectra due to partial charge transfer to the nanotube from the nucleic acid base. In our case, a charge of 0.09e is transferred to CNT (5, 0) from guanine (Table 1); this validates the higher binding energy of guanine with the narrow tube rather than the wide tubes. The high curvature surface and the increased electronegativity of CNT (5, 0) drag more electrons towards it [10]. In the other cases, there is no significant charge transfer.

In some earlier works, charge transfer between the CNT and the nucleic acid base was calculated [11, 14, 17, 18] and isosurface plots [11, 17] were examined. Physisorption of nucleic acid bases with CNT occurs due to the interaction between the π electron clouds. Thus, by concentrating on the complete charge density profile of CNT and nucleic acid bases, we will be able to give a better interpretation about the nature of the interaction between them. We analyzed [33] the highest occupied molecular orbital (HOMO) and lowest unoccupied molecular orbital (LUMO) surfaces of CNT and nucleic acid bases. Here, we present the results of two important as well as unique cases: adsorption of guanine on CNT (5, 0) and adsorption of thymine on CNT (10, 0). Figure 3 shows the charge density distribution of the isolated guanine molecule and CNT (5, 0) guanine hybrid.

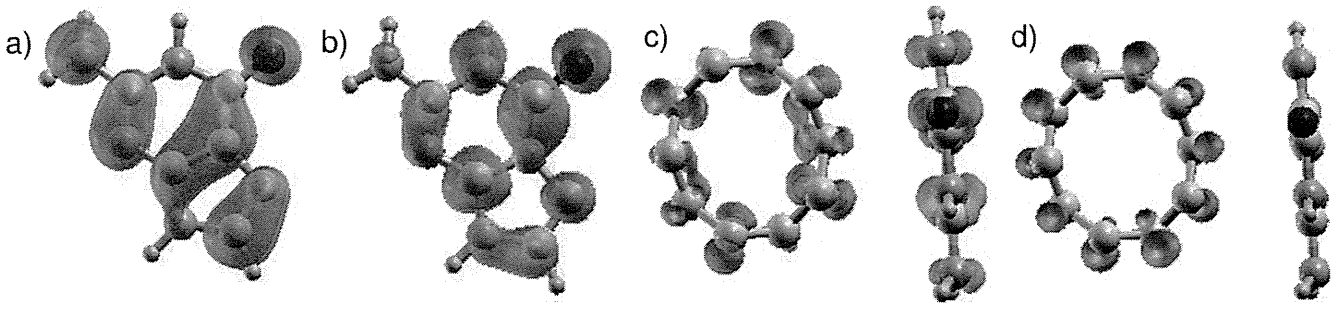

Fig. 3a–d Charge distribution in the CNT (5, 0) guanine hybrid. **a** Highest occupied molecular orbital (HOMO) of isolated guanine. **b** Lowest unoccupied molecular orbital (LUMO) of isolated guanine. **c** HOMO of CNT (5, 0) guanine hybrid. **d** LUMO of CNT (5, 0) guanine hybrid

Charge density is concentrated on the C–C and C–N bonds of the isolated HOMO guanine (Fig. 3a), and in LUMO (Fig. 3b) it spreads over all the atoms. Contribution of the delocalized π electrons of the CNT in the interaction is clearly visible in the bottom panel pictures. Contraction of the CNT diameter near the adsorption field disturbs the π electron distribution over the carbon atoms (Fig. 3c). Thus there is depletion in the charge density of HOMO, whereas in LUMO charge is distributed homogeneously throughout the CNT (Fig. 3d). HOMO charge density concentrated on the guanine triggers physisorption with CNT. Charge accumulated on the oxygen and C–N bonds of guanine induces charge transfer to CNT. HOMO and LUMO of isolated thymine and the CNT (10, 0) thymine hybrid are presented in Fig. 4. In the HOMO of the isolated molecule (Fig. 4a), the charge density is evenly distributed over the carbon, nitrogen and oxygen atoms. Accurate geometry optimization plays a crucial role in the study of non-covalent interactions. During the adsorption of thymine on CNT (10, 0), thymine tilts towards the CNT along the side with two oxygen atoms. In the HOMO (Fig. 4c) of CNT (10, 0)+Thymine, a large collection of π electron density is gathered on the CNT near the thymine. Also, some small amount of charge accumulates on the base. Thus, the interaction between the π electron clouds is repulsive, and reduces the binding strength between the two entities.

Electronic band structure and density of state analysis

Generally, the electronic property of a CNT is not modified by physisorption of the adsorbate [11, 17]. Figure 5 shows the electronic band structure and density of states plots for the CNT (5, 0) and CNT (5, 0) guanine hybrid and CNT (5, 0) thymine hybrid, respectively. Intrinsic CNT exhibits metallic characteristics; the adsorption of neither guanine nor thymine changes the electronic properties of CNT (5, 0). However, the adsorption of the nucleic acid bases introduced additional bands below −0.5 eV in the intrinsic CNT band structure. In the DOS plot, no changes were observed at the Fermi level, confirming that the adsorption of nucleic acid bases on CNT is a simple superposition of individual systems without hybridization of orbitals. This holds true for all the other cases too.

Interaction of guanine thymine pair with CNT (5, 0)

In addition to the study of the adsorption of isolated bases on CNT, adsorption of a single guanine-thymine (GT) wobble base pair on CNT (5, 0) was investigated. A GT wobble base pair is formed with two hydrogen bonds between the O–H–N atoms of the bases [8]. Zheng et al. [6, 7] proposed CNT sorting mediated through a poly GT oligonucleotide formed by a non-Watson-Crick hydrogen bond network. A study of adsorption of a GT dimer on

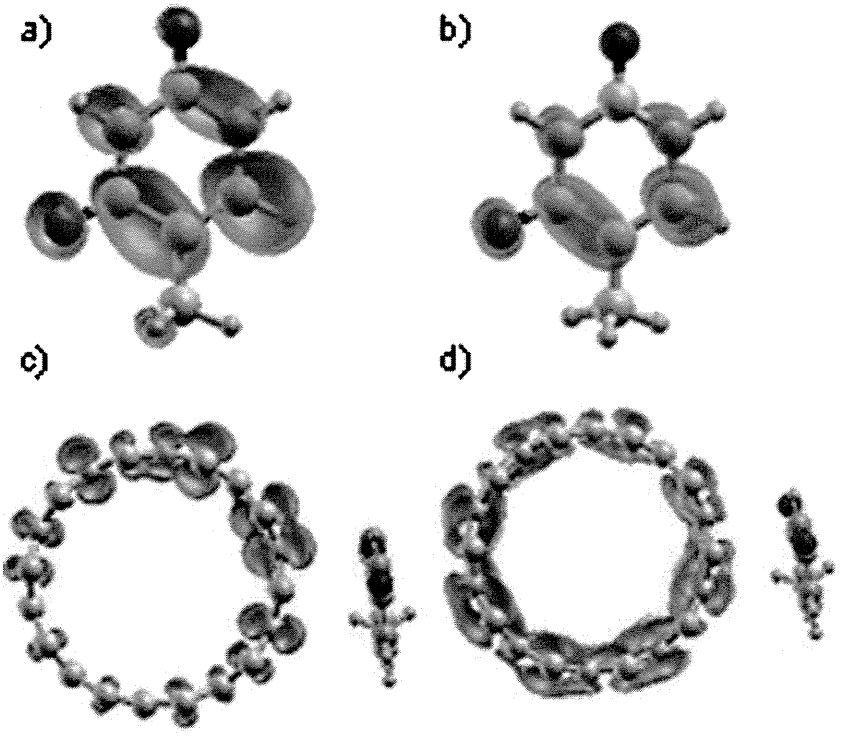

Fig. 4a–d Influence of the intermolecular separation in the charge accumulation and depletion in CNT (10,0) thymine hybrid. **a** HOMO of isolated thymine. **b** LUMO of isolated thymine. **c** HOMO of CNT (10, 0) thymine hybrid. **d** LUMO of CNT (10, 0) thymine hybrid

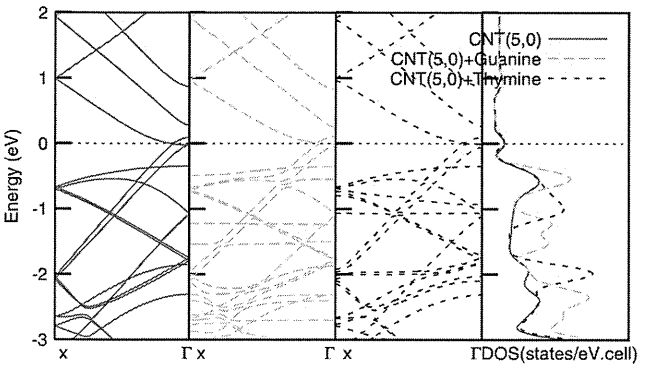

Fig. 5 Comparison between the band structure and density of states of CNT (5, 0), CNT (5, 0) guanine hybrid and CNT (5, 0) thymine hybrid

(11, 0) SWCNT revealed that, due to the stress induced within the ssDNA sugar residues and glycosidic bonds during optimization, the structural geometry was altered and became unstable [8]. In our study, the sugar phosphate backbone of DNA is not taken into account. Initially, the GT base pair is placed parallel to the CNT in the *z*-axis direction. The optimization process rearranged the initial parallel orientation of the base pair. The oxygen- and nitrogen-enriched middle portion of the nucleic acid base pair is moved away from the CNT (Fig. 6). Binding energy of the π–π stacked system is expected to increase in proportional with the π electron surface [30]. The calculated binding energy of the GT base pair with CNT (5, 0) is 0.36 eV. In comparison with the binding energy of isolated guanine (0.41 eV) and thymine (0.20 eV) with CNT (5, 0), the binding strength of the guanine thymine base pair on CNT (5, 0) is relatively weak. Charge density analysis has shown a charge transfer of 0.1e to the CNT from the base pair. The electronic charge density plots of HOMO and LUMO are presented in Fig. 6. In the HOMO (Fig. 6a), charge is distributed over the CNT and oxygen, nitrogen atoms of the nucleic acid bases. Charge of the LUMO (Fig. 6b) is distributed evenly on CNT, which establishes the metallic nature of the tube.

Conclusions

We have studied the interaction mechanism of the nucleic acid bases guanine and thymine with four different CNTs. Apart from the curvature effect of CNT, orientation of the nucleic acid bases and intermolecular distance between CNT and nucleic acid base play a predominant role in deciding the binding strength, which in turn influences charge transfer. Most importantly, the π–π stacking interaction is affected by the intermolecular distance between the CNT and the nucleic acid base. The binding strength of the nucleic acid base is reduced due to the exchange-repulsive interaction of the π–π charge cloud when the intermolecular distance between the adsorbent and adsorbate is less than the characteristic π–π stacking separation. However, the resultant π–π stacking interaction is attractive. When comparing the results obtained for guanine and thymine, the interaction energy of guanine is higher than that of thymine for all the CNTs tested. The role of van der Waals interactions in determining the magnitude of the π–π interaction energy is directly proportional to the area of the π overlap [30]. In addition to the pyrimidine ring of thymine, guanine has a fused imidazole ring and more electronegative nitrogen atoms, increasing the area of π surface of the adsorbate, which enhances the interaction. The binding energy of the adsorbate increases as the diameter of the CNT increases. However, this is not true in the case of guanine adsorption on CNT (5, 0) and thymine adsorption on CNT (10, 0). The high curvature of the narrow CNT (5, 0) drags more electrons towards it, and the contraction of the CNT facilitates the interaction of π electron clouds. This explains the higher binding energy of guanine with the narrow tube rather than the wide tubes. In

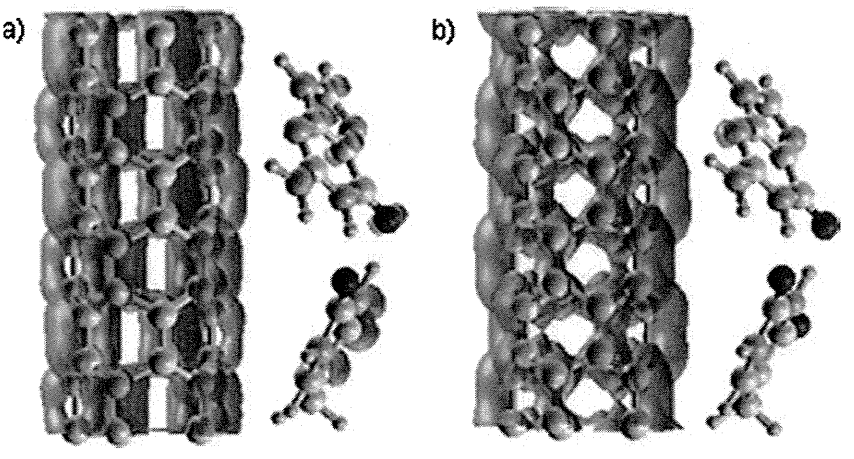

Fig. 6a,b Intermolecular interaction of CNT (5, 0) guanine thymine hybrid. **a** HOMO of CNT (5, 0) guanine thymine hybrid. **b** LUMO of CNT (5, 0) guanine thymine hybrid

the case of CNT (10, 0), the short intermolecular separation between thymine and CNT (10, 0) leads to the reduced binding energy of thymine because of the increased π–π repulsive interaction. Our results confirm that DFT-LDA can forecast the intermolecular separations and binding energies of non-covalent systems. Modeling a bio-nano hybrid like a non-covalently adsorbed nucleic acid base on CNT can lead to the utilization of CNT as a sensor or as a transporter for drugs and genes.

Acknowledgments The University Grants Commission is acknowledged for supporting this project with a junior research fellowship, under University with Potential for Excellence. K.I. acknowledges the financial support of the Council of Scientific and Industrial Research under the Emeritus Scientist Scheme. The authors would like to express their sincere thanks to the crew of the Center for Computational Materials Science at the Institute for Materials Research, Tohoku University, for their continuous support of the SR11000 supercomputing facilities.

References

1. Lu Q, Moore JM, Huang G, Mount AS, Rao AM (2004) RNA polymer translocation with single-walled carbon nanotubes. Nano Lett 4:2473–2477
2. Kam NWS, Dai H (2005) Carbon nanotubes as intracellular protein transporters: generality and biological functionality. J Am Chem Soc 127:6021–6026
3. Chen RJ, Bangsarunzip S, Drouvalakis KA, Shi Kam NW, Shim M, Li Y, Kim W, Utz PJ, Dai H (2003) Noncovalent functionalization of carbon nanotubes for highly specific electronic biosensors. Proc Natl Acac Sci USA 100:4984–4989
4. Kuang Z, Kim SN, Crookes-Goodson WJ, Farmer BL, Naik RR (2010) Biomimetic chemosensor: designing peptide recognition elements for surface functionalization of carbon nanotube field effect transistors. ACS Nano 4:452–458
5. Zheng M, Jagota A, Semke ED, Diner BA, Mclean RS, Lustig SR, Richardson RE, Tassi NG (2003) DNA-assisted dispersion and separation of carbon nanotubes. Nat Mater 2:338–342
6. Zheng M, Jagota A, Strano MS, Santos AP, Barone P, Chou SG, Diner BA, Dresselhaus MS, Mclean RS, Onoa GB, Samsonidze GG, Semke ED, Usrey M, Walls DJ (2003) Structure based carbon nanotube sorting by sequence-dependent DNA assembly. Science 302:1545–1548
7. Tu X, Zheng M (2008) A DNA based approach to the carbon nanotube sorting problem. Nano Res 1:185–194
8. Johnson RR, Charlie Johnson AT, Klein ML (2008) Probing the structure of DNA-carbon nanotube hybrids with molecular dynamics. Nano Lett 8:69–75
9. Lu G, Maragakis P, Kaxiras E (2005) Carbon nanotube interaction with DNA. Nano Lett 5:897–900
10. Meng S, Maragakis P, Papaloukas C, Kaxiras E (2007) DNA nucleoside interaction and identification with carbon nanotubes. Nano Lett 7:45–50
11. Gowtham S, Scheicher RH, Pandey R, Karna SP, Ahuja R (2008) First-principles study of physisorption of nucleic acid bases on small diameter carbon nanotubes. Nanotechnology 19 (6):125701
12. Shukla MK, Dubey M, Zakar E, Namburu R, Czyznikowska Z, Leszczynski J (2009) Interaction of nucleic acid bases with single-walled carbon nanotube. Chem Phys Lett 480:269–272
13. Stepanian SG, Karachevtsev MV, Glamazda AY, Karachevtsev VA, Adamowicz L (2009) Raman spectroscopy study and first-principles calculations of the interaction between nucleic acid bases and carbon nanotubes. J Phys Chem A 113:3621–3629
14. Das A, Sood AK, Maiti PK, Das M, Varadarajan R, Rao CNT (2008) Binding of nucleobases with single-walled carbon nanotubes: theory and experiment. Chem Phys Lett 453:266–273
15. Frischknecht AL, Martin MG (2008) Simulation of the adsorption of nucleotide monophosphates on carbon nanotubes in aqueous solution. J Phys Chem C 112:6271–6278
16. Martin W, Zhu W, Krilov G (2008) Simulation study of noncovalent hybridization of carbon nanotubes by single-stranded DNA in water. J Phys Chem B 112:16076–16089
17. Shtogun YV, Woods LM, Dovbeshko GI (2007) Adsorption of adenine and thymine and their radicals on single-wall carbon nanotubes. J Phys Chem C 111:18174–18181
18. Wang Y (2008) Theoretical evidence for the stringer ability of thymine to disperse SWCNT than cytosine adenine: self stacking bases vs their cross stacking with SWCNT. J Phys Chem C 112:14297–14305
19. Kresse G, Furthmuller J (1996) Efficient iterative schemes for ab initio total-energy calculations using a plane-wave basis set. Phys Rev B 54:11169–11186
20. Kresse G, Furthmuller J (1996) Efficiency of ab initio total energy calculations for metals and semiconductors using a plane-wave basis set. Comput Mater Sci 6:15–50
21. Blochl PE, Kresse G, Joubert J (1999) Projected augmented-wave method. From ultrasoft pseudopotentials to the projector augmented-wave method. Phys Rev B 50:17953–17979
22. Perdew JP, Zunger A (1981) Self-interaction correction to density-functional approximations for many-electron systems. Phys Rev B 23:5048–5079
23. Perdew JP, Chevary JA, Vosko SH, Jackson KA, Pederson MR, Singh DJ, Fiolhais C (1992) Atoms, molecules, solids, and surfaces: applications of the generalized gradient approximation for exchange and correlation. Phys Rev B 46:6671–6687
24. Girifalco LA, Hodak M (2002) Van der Waals binding energies in graphitic structures. Phys Rev B 65(1):125404
25. Tournus F, Latil S, Heggie MI, Charlier JC (2005) π-stacking interaction between carbon nanotubes and organic molecules. Phys Rev B 72(5):075431
26. Ortmann F, Schmidt WG, Bechstedt F (2005) Attracted by long range electron correlation: adenine and graphite. Phys Rev Lett 95 (4):186101
27. Lim S, Park N (2009) Ab initio study of noncovalent sidewall functionalization of carbon nanotubes. Appl Phys Lett 95(3):243110
28. Monkhorst HJ, Pack JD (1976) Special points for brillouin-zone integrations. Phys Rev B 13:5188–5192
29. Liu Z, Sun X, Nakayama-Ratchford N, Dai H (2007) Supramolecular chemistry on water-soluble carbon nanotubes for drug loading and delivery. ACS Nano 1:50–56
30. Hunter CA, Sanders JKM (1990) The nature of π–π interactions. J Am Chem Soc 112:5525–5534
31. Jeziorski B, Moszynski R, Szalewicz K (1994) Perturbation theory approach to intermolecular potential energy surfaces of van der Waals complexes. Chem Rev 94:1887–1930
32. Henkelman G, Arnaldsson A, Jonsson H (2006) A fast and robust algorithm for Bader decomposition of charge density. Comput Mater Sci 36:254–360
33. Kokalj A (2003) Computer graphics and graphical user interfaces as tools in simulations of matter at the atomic scale. Comput Mater Sci 28:155–168

◆ Human Brain Mapping 33:552–568 (2012) ◆

Age-Related Changes in Topological Organization of Structural Brain Networks in Healthy Individuals

Kai Wu,[1]* Yasuyuki Taki,[1,2] Kazunori Sato,[1] Shigeo Kinomura,[1] Ryoi Goto,[1] Ken Okada,[1] Ryuta Kawashima,[2,3] Yong He,[4,5] Alan C. Evans,[5] and Hiroshi Fukuda[1]

[1]*Department of Nuclear Medicine and Radiology, Institute of Development, Aging and Cancer, Tohoku University, Sendai, Japan 980-8575*
[2]*Division of Developmental Cognitive Neuroscience, Institute of Development, Aging and Cancer, Tohoku University, Sendai, Japan 980-8575*
[3]*Department of Functional Brain Imaging, Institute of Development, Aging and Cancer, Tohoku University, Sendai, Japan 980-8575*
[4]*State Key Laboratory of Cognitive Neuroscience and Learning, Beijing Normal University, Beijing, China 100875*
[5]*McConnell Brain Imaging Centre, Montreal Neurological Institute, McGill University, Montreal, QC, Canada H3A 2B4*

Abstract: The aim of this study was to examine structural brain networks using regional gray matter volume, as well as to investigate changes in small-world and modular organization with normal aging. We constructed structural brain networks composed of 90 regions in young, middle, and old age groups. We randomly selected 350 healthy subjects for each group from a Japanese magnetic resonance image database. Structural brain networks in three age groups showed economical small-world properties, providing high global and local efficiency for parallel information processing at low connection cost. The small-world efficiency and node betweenness varied significantly and revealed a U- or inverted U-curve model tendency among three age groups. Results also demonstrated that structural brain networks exhibited a modular organization in which the connections between regions are much denser within modules than between them. The modular organization of structural brain networks was similar between the young and middle age groups, but quite different from the old group. In particular, the old group showed a notable decrease in the connector ratio and the intermodule connections. Combining the results of small-world efficiency, node betweenness and modular organization, we concluded that the brain network changed slightly, developing into a more distributed organization from young to middle age. The organization eventually altered greatly, shifting to a more localized organization in old age. Our findings provided quantitative insights into topological principles of structural brain networks and changes related to normal aging. *Hum Brain Mapp 33:552–568, 2012.* © 2011 Wiley Periodicals, Inc.

Key words: structural brain network; economical small-world; modular organization; normal aging; regional gray matter volume; magnetic resonance imaging

Additional Supporting Information may be found in the online version of this article.

Contract grant sponsor: 2007 Tohoku University Global COE Program "Global Nano-Biomedical Engineering Education and Research Network Centre"; the MEXT Grant-in-Aid for Scientific Research on Innovative Areas, 22103501.

*Correspondence to: Kai Wu, Institute of Development, Aging and Cancer, Tohoku University, Sendai, Japan 980-8575.
E-mail: kaiwu@idac.tohoku.ac.jp

Received for publication 28 September 2009; Revised 24 October 2010; Accepted 18 November 2010
DOI: 10.1002/hbm.21232
Published online 9 March 2011 in Wiley Online Library (wileyonlinelibrary.com).

INTRODUCTION

New advances in the quantitative analysis of complex networks, based largely on graph theory, have been rapidly applied to studies of brain network topological organization. The structural and functional systems of the human brain show topological properties of complex networks, such as small-world properties, highly connected hubs, and modularity [Bullmore and Sporns, 2009]. Significant discoveries related to human brain functional networks have indicated that the brain exhibits small-world properties characterized by a high clustering index and a short average distance between any two regions [Latora and Marchiori, 2001; Watts and Strogatz, 1998], using modern neuroimaging techniques such as functional magnetic resonance imaging (fMRI), and electroencephalogram (EEG) [Achard and Bullmore, 2007; Achard et al., 2006; Bassett et al., 2006; Eguiluz et al., 2005; Ferri et al., 2007; Micheloyannis et al., 2006; Salvador et al., 2005]. It has been verified that structural networks of the human brain revealed by measurements of cortical thickness or regional gray matter volume (RGMV) have small-world properties [Bassett et al., 2008; He et al., 2007, 2008, 2009a]. Moreover, the small-world properties were confirmed in human brain structural networks using diffusion MRI technique [Gong et al., 2009b; Hagmann et al., 2007; Iturria-Medina et al., 2008]. Achard and Bullmore were the first to demonstrate economical small-world properties in brain functional networks, which provide high global and local efficiency for parallel information processing at a low wiring cost [Achard and Bullmore, 2007]. Efficiency metrics have also provided a new measure to quantify differences between patient groups and appropriate comparison groups [He et al., 2009a; Liu et al., 2008; Wang et al., 2009b].

Modularity is thought to be one of the main organizing principles in most complex systems, including biological, social, and economical networks [Girvan and Newman, 2002; Guimerà et al., 2005; Hartwell et al., 1999; Newman, 2006a]. A key advantage of modular organization is that it favors evolutionary and developmental optimization of multiple or changing selection criteria: a modular-organized network can evolve or grow one module at a time, without risking loss of function in other modules [Kashtan and Alon, 2005; Redies and Puelles, 2001]. Defining and characterizing modular organization in the human brain can help us to identify a set of modules structurally or functionally associated with components that perform specific biological functions. This investigation will also provide us with rich quantitative insights into structural–functional mapping. The modular organization of structural and functional networks in human brain has been demonstrated by several previous studies [Chen et al., 2008; Ferrarini et al., 2009; Hagmann et al., 2008; He et al., 2009b; Meunier et al., 2009a,b; Robinson et al., 2009; Valencia et al., 2009].

Normal processes of brain maturation and senescence might be reflected as quantifiable changes in structural and functional network topological properties [Bullmore and Sporns, 2009; Micheloyannis et al., 2009]. A previous study on functional brain networks indicated that an older age group had significantly reduced cost efficiency in comparison to a younger group [Achard and Bullmore, 2007]. Normal aging might thus be associated with changes in the economical small-world properties of brain functional networks. Furthermore, normal aging had been proven to be associated with changes in modular organization of human brain functional networks [Meunier et al., 2009a]. A recent study reported that the organization of multiple functional brain networks shifts from a local anatomical emphasis in children to a more distributed organization in young adults [Fair et al., 2009]. The study also demonstrated that community detection by modularity optimization reveals stable communities within the graphs that are clearly different between young children and young adults [Fair et al., 2009]. A recent study also reported that the development of large-scale brain networks is characterized by weakening of short-range functional connectivity and strengthening of long-range functional connectivity, comparing the children group (7–9 years) with the young-adults group (19–22 years), [Supekar et al., 2009]. However, few studies have analyzed the influences on both small-world and modular organization with normal aging. The main purpose of this study is to clarify topological properties in structural brain networks among different age groups. We hypothesized that the economical small-world properties and the modular organization of structural brain networks would be altered with normal aging.

In the present study, we divided all healthy subjects into three groups by age. Study participants were selected from a large-scale brain MRI database of normal Japanese (1421 subjects, ages from 18 to 80 years), [Sato et al., 2003]. The structural connectivity in the human brain consisting of 90 regions was constructed by computing the correlation matrix of RGMV across subjects within each group. Efficiency metrics were applied to investigate whether structural brain networks show economical small-world attributes and whether significant differences exist in properties of brain networks among three age-specific groups. We investigated the regional nodal characteristics of brain networks and compared the between-group differences in node betweenness. Furthermore, we examined the modular organization of structural brain networks and identified several modules of the brain network in each age-specific group. To clarify differences on the modular organization of brain networks among three groups, we compared the constitution of modules and computed attributes using, for example, the connector ratio and the distribution efficiency.

MATERIALS AND METHODS

Subjects

The subjects were all community-dwelling normal Japanese subjects recruited by two projects; the Aoba Brain

TABLE I. Characteristics of the subjects

Group ID	Age range	Number of subjects	Age (mean ± SD)
Young (Y)	18–40	551 (F: 231/M: 320)	27.42 ± 6.77
		350 (F: 158/M: 192)	***27.31 ± 6.65***
Middle (M)	41–60	560 (F: 331/M: 229)	50.94 ± 5.22
		350 (F: 196/M: 154)	***51.07 ± 5.26***
Old (O)	61–80	372 (F: 198/M: 174)	68.32 ± 4.58
		350 (F: 188/M: 162)	***68.17 ± 4.03***

The italic and bold characters indicate the characteristics of 350 subjects randomly selected for each group.

Imaging Project, Sendai, Japan and the Tsurugaya Project, Sendai, Japan. The Aoba Brain Imaging Project was performed to create a database of normal Japanese brain images [Sato et al., 2003]. To perform this, we obtained 1,637 brain MR images from normal Japanese volunteers who were living in and around Sendai City, Japan. The Tsurugaya Project study is a comprehensive geriatric assessment (CGA) of the elderly population. It involved 1,179 subjects aged 70 years or older in 2002 who were living in Tsurugaya district, Sendai City, Japan. We selected 210 subjects by random sampling from subjects who would be willing to undergo brain MRI and submitted these patients to MRI. The subjects of the two projects were all healthy and had neither present illness nor a history of neurological disease, psychiatric disease, brain tumor, or head injury. Prior to the acquisition of MR images, all subjects enrolled in the two projects were interviewed by medical doctors for screening to determine whether he/she was normal and to obtain clinical data. In both projects, we excluded in advance those subjects who had past or present history of malignant tumors, head traumas, cerebrovascular diseases, epilepsy, or psychiatric diseases. After the interview, brain MR images were obtained from each subject. The MR images were inspected by two to three well-trained radiologists. Images with the following findings were excluded from this study: head injuries, brain tumors, hemorrhage, major and lacunar infarctions, and moderate to severe white matter hyperintensities. We did not exclude the images with mild spotty white matter hyperintensities.

We collected brain images of 1,483 subjects in this study (mean ± S.D.; age, 46.30 ± 16.98 years; range: 18–80 years). To investigate the topological properties and organization of structural brain networks with normal aging, we divided all subjects into three groups by age (young, 18–40 years; middle, 41–60 years; old, 61–80 years), without regard to sex. Group ID naming and characteristics of the subjects are shown in Table I.

MRI data acquisition and the use of them for the studies by Fukuda H (the last author of the study) were approved by the Institutional Review Board of Tohoku University School of Medicine. Informed consent was obtained from each subject after a full explanation of the purpose and procedures of the study, according to the Declaration of Helsinki (1991), prior to MR image scanning.

Image Acquisition

Brain images were obtained from each subject using two 0.5 T MR scanners (Sigma contour, GE-Yokogawa Medical Systems, Tokyo) with two different pulse sequences: (1) 124 contiguous, 1.5-mm thick axial planes of three dimensional T1-weighted images (spoiled gradient recalled acquisition in steady state: repetition time (TR), 40 ms; echo time (TE), 7 ms; flip angle (FA), 30°; voxel size, 1.02 mm × 1.02 mm × 1.5 mm); (2) 63 contiguous, 3 mm-thick axial planes of gapless (using interleaving) proton density-weighted images/T2-weighted images (dual echo fast spin echo: TR, 2,860 ms; TE, 15/120 ms; voxel size, 1.02 mm × 1.02 mm × 3 mm). T1 images were used for the present analysis and all three images were used to exclude those MRIs with abnormalities, as described above.

Measurements of Regional Gray Matter Volume

After the image acquisition, RGMV for each subject was measured by using statistical parametric mapping 2 (SPM2) (Wellcome Department of Cognitive Neurology, London, UK) [Friston et al., 1995] in Matlab (Math Works, Natick, MA). First, T1-weighted MR images were transformed to the same stereotactic space by registering each of the images to the ICBM 152 template (Montreal Neurological Institute, Montreal, Canada), which approximates the Talairach space [Jean Talairach, 1988]. Then, tissue segmentation from the raw images to the gray matter, white matter, cerebrospinal fluid space, and non-brain tissue was performed using the SPM2 default segmentation procedure. We applied these processes using the MATLAB file "cg_vbm_optimized" (http://dbm.neuro.uni-jena.de/vbm.html). WFU_PickAtlas software was employed to label the regions in the gray matter images, which provided a method for generating ROI masks based on the Talairach Daemon database [Lancaster et al., 2000; Maldjian et al., 2003, 2004]. We parcellated the entire gray matter into 45 separate regions for each hemisphere (90 regions in total, see Supporting Information Table SI) defined by the Automated Anatomical Labeling (AAL) atlas [Tzourio-Mazoyer et al., 2002] to calculate the RGMV for each subject.

Construction of Brain Structural Connection Matrix

To study the topological properties of structural brain networks among three age-specific groups, we examined the correlation matrices using graph-theoretical analysis: GroupIDs were Young, Middle, and Old. Since there was a large difference in the number of subjects in each group, we randomly selected 350 subjects for each age group (the original group) (Table I) to reduce the influence due to varying degrees of freedom for each group in computing inter-regional correlation across subjects. We also repeated this randomly-selected grouping method 20 times in each age group to examine whether subject characteristics were

TABLE II. Topological parameters of structural brain networks used in this study

Network properties	Characters	Descriptions
Economical small-world properties	Cost	The cost or the sparsity to construct a network.
	Eloc	The local efficiency measures how efficient are the network to exchange the information at the clustering level.
	Eglob	The global efficiency measures how efficient are the network to exchange the information at the global level.
	I_{Eloc}	The integrated local efficiency is the integrals of the local efficiency curves over the preselected range of cost threshold.
	I_{Eglob}	The integrated global efficiency is the integrals of the global efficiency curves over the preselected range of cost threshold.
Nodal characteristics	BC	The normalized betweenness measures the ability of a node relative to information flow between other nodes throughout the network.
	I_{BC}	The integrated normalized betweenness is the integrated normalized betweenness over the preselected range of cost threshold.
Modularity	B	The modularity measures how the network is organized into modules with high level of local clustering.
	sBC	The within-module betweenness centrality measures the importance of a node relative to the information flow between other nodes in the module.
	PC	The participant coefficient measures the ability of a node to maintain the communication between its own module and the other modules.

significantly changed. As a result, the characteristics of 350 subjects randomly selected for each age group were not significantly different from those of the original group. We used a linear regression analysis to remove the effects from total gray matter volume and sex, so that the residuals of this regression were employed as the substitute for the raw RGMV, denoted as corrected RGMV (cRGMV). To analyze the structural brain network by using RGMV, we first applied the method introduced by He et al. to construct the structural connection matrix [He et al., 2007]. We computed the Pearson correlation coefficient between cRGMV across 350 subjects randomly chosen from each group to construct the interregional correlation matrix ($N \times N$, where N is the number of gray matter regions, here $N = 90$) for each group. Each connection matrix can be converted to a binarized and undirected graph (network) G by using a correlation or cost threshold. Then the networks were analyzed by using graph theoretical methods. All topological parameters of the networks calculated in this study and their implications are shown in Table II.

Small-World Properties

Small-world properties (clustering coefficient, C_p and characteristic path length, L_p) were originally defined by Wattz and Strogatz [1998]. In addition to the conventional small-world parameters (C_p and L_p), more biologically sensible properties of brain networks are the efficiency metrics (global efficiency, E_{glob} and local efficiency, E_{loc}), which measure the capability of the network with regard to information transmission at the global and local levels, respectively [Latora and Marchiori, 2001]. In several recent studies, the efficiency metrics have been applied to human brain functional [Achard and Bullmore, 2007; Wang et al., 2009a,b] and structural [He et al., 2009a; Iturria-Medina et al., 2008] network studies. For a graph G with N nodes and K edges, the global efficiency of G can be computed as [Latora and Marchiori, 2001]:

$$E_{glob}(G) = \frac{1}{N(N-1)} \sum_{i \neq j \in G} \frac{1}{d_{ij}} \quad (1)$$

where d_{ij} is the shortest path length between node i and node j in G. The local efficiency of G is defined as [Latora and Marchiori, 2001]:

$$E_{loc}(G) = \frac{1}{N} \sum_{i \in G} E_{glob}(Gi) \quad (2)$$

where $E_{glob}(G_i)$ is the global efficiency of G_i, the sub-graph of the neighbors of node i. In this study, we generated a population (n 1,000) of regular networks and random networks that preserved the same number of nodes and edges, respectively. The efficiency metrics (E_{glob} and E_{loc}) of real brain networks (G) were compared with those of regular graphs (G_{reg}) and random graphs (G_{rand}), respectively. The real brain network G is considered to be a small-world network if it meets the following criteria [Latora and Marchiori, 2001]:

$$E_{glob}(G_{reg}) < E_{glob}(G) < E_{glob}(G_{rand}) \; and \; E_{loc}(G_{rand}) < E_{loc}(G) < E_{loc}(G_{reg}) \quad (3)$$

In this study, we applied a cost threshold to investigate economical small-world properties of networks. Such a thresholding approach can normalize all networks to have

the same number of edges or wiring cost and thus provide an avenue to detect changes in topological organization with aging [Achard and Bullmore, 2007; He et al., 2009a]. To estimate the small-world properties of structural brain networks and to define a small-world regime, we first applied a broad cost threshold range ($0.05 \leq$ cost ≤ 0.5, increased by 0.01) to all the connection matrices. The cost (or sparsity) was computed as the ratio of the number of actual connections divided by the maximum possible number of connections in the network. We then adopted the following complementary approaches to choose the small-world regime: (1) the small-world properties were estimable ($K > \log(N) = 4.5$, $N = 90$) [Watts and Strogatz, 1998], (2) all brain networks were fully connected, and (3) the resulting brain networks have sparse properties and distinguishable properties in comparison to the degree-matched random networks [Bassett et al., 2008; Liu et al., 2008; Wang et al., 2009a]. Finally, we selected the small-world regime as a range of cost threshold ($0.11 \leq$ cost ≤ 0.25, step = 0.01). These thresholds were also used for the following calculation of regional nodal characteristics and modularity.

Regional Nodal Characteristics

In this study, we examined the node betweenness in the networks. The betweenness bc_i of a node i is defined as the number of shortest paths between any two nodes that run through node i [Freeman, 1977]. We defined the normalized betweenness as $BC_i = bc_i/\langle bc_i \rangle$, where $\langle bc_i \rangle$ was the average betweenness of all nodes. Thus, the normalized betweenness of BC_i measures the ability of a node relative to information flow between other nodes throughout the network. Finally, we averaged the normalized betweenness across the range of cost threshold ($0.11 \leq$ cost ≤ 0.25). Regions with a higher value of $\overline{BC_i}$ (> mean + SD) were identified as global hubs in the brain network [Sporns et al., 2007].

Modularity and Regional Role

A module can be generally defined as a subset of nodes in the graph that are more densely connected to the other nodes in the same module than to nodes outside the module [Radicchi et al., 2004]. Several algorithms have been proposed to define the modular decomposition of an undirected graph [Clauset et al., 2004; Danon et al., 2005; Guimerà and Amaral, 2005a, 2005b; Guimerà et al., 2004; Newman 2006a, 2006b, 2004; Newman and Girvan, 2004; Reichardt and Bornholdt, 2006]. Despite the many interesting alternative methods, it should be noted that the problem of community finding remains a challenge because no single method is fast and sensitive enough to ensure ideal results for general, large networks, a problem that is compounded by the lack of a clear definition of communities. Here, we adopted the spectral algorithm [Guimerà and Amaral, 2005b; Guimerà et al., 2004; Newman, 2006a] for community detection, which is believed to be the most precise and be able to find a division with the highest value of modularity for many networks [Costa et al., 2007]. This algorithm reformulates the modularity concept in terms of the eigenvectors of a new characteristic matrix for the network, called the modularity matrix [Newman, 2006a].

For each subgraph g, its modularity matrix $B^{(g)}$ has elements

$$b_{ij}^{(g)} = a_{ij} - \frac{k_i k_j}{2M} - \delta_{ij} \sum_{u \in N(g)} \left[a_{iu} - \frac{k_i k_u}{2M} \right] \quad (4)$$

for vertices i and j in g. In Eq. (4), the actual number of edges falling between a particular pair of vertices i and j is aij; k_i is the degree of a vertex i; $\delta_{ij} = 1$ if $i = j$ and 0 otherwise. Thus, to split the network in communities, the modularity matrix is constructed and its most positive eigenvalue and corresponding eigenvector are determined. According to the signs of the elements of this vector, the network is divided in two parts (vertices with positive elements are assigned to one community and vertices with negative elements to another). Next, the process is repeated recursively to each community until a split that makes a zero or negative contribution to total modularity is reached. Similarly, Newman proposed a new definition of communities as indivisible subgraphs, i.e., subgraphs whose division would not increase the modularity.

In this study, we detected the community structure for the structural brain networks of three groups, which were thresholded by a specific cost threshold (cost = 0.11). With this threshold, we can capture the structural connectivity backbone underlying the modular organization of the most sparse and fully-connected brain networks. To further distinguish the roles of nodes in terms of their intra- and inter-module connectivity patterns, the two measurements, the within-module betweenness centrality, sBC and the participant coefficient (PC) were applied [Guimerà and Amaral, 2005a; Guimerà et al., 2005]. The sBC (i) of a node i is the betweenness centrality, but is calculated only within the module s to which it belongs. This parameter measures the importance of a node relative to the information flow between other nodes in the module. The PC(i) of a node i is defined as

$$PC(i) = 1 - \sum_{s=1}^{N_M} \left(\frac{k_{is}}{k_i} \right)^2$$

where N_M is the number of modules, k_{is} is the number of links of node i to nodes in module s and k_i is the total degree of node i. The PC(i) tends to 1 if node i has a homogeneous connection distribution with all the modules and to 0 if it does not have any inter-module connections. PC measures the ability of a node to maintain the

communication between its own module and the other modules. A high PC value for a given node usually means the node has many inter-module connections. Depending on the sBC, the nodes in the brain functional network were classified as modular hubs (sBC >mean + std) or non-hubs (sBC ≤mean + std), respectively. In terms of the PC, the hub nodes were further subdivided into R1 connector hubs (PC > 0.25) and R2 provincial hubs (PC ≤ 0.25), and non-hub nodes were divided into R3 connector non-hubs (PC > 0.25) and R4 peripheral non-hubs (PC ≤ 0.25) [Guimerà and Amaral, 2005a; Guimerà, 2005].

Statistical Analysis

To analyze statistical significance of between-group differences with regard to the efficiency metrics (local and global efficiency) among three age-specific groups, a nonparametric permutation test method was applied in the small-world regime defined above (0.11 ≤cost ≤0.25, step = 0.01), [Bullmore et al., 1999; He et al., 2008]. Thus, we can explore the between-group differences in efficiency metrics at each threshold level. Here, we performed three comparisons (Z_I, Z_{II}, Z_{III}) including the young versus middle (Y vs. M), the middle versus old (M vs. O), and the young versus old (Y vs. O), respectively. For each comparison, the efficiency metrics of binarized graphs at a given threshold were computed separately for each group. Then one randomization procedure of the permutation test yielded two new groups that were generalized by randomly reallocating each subject's set of cRGMV measures from previous groups. The correlation matrices for new groups were recomputed and binarized by thresholding to achieve the same threshold as in the real networks. The efficiency metrics of corresponding binarized graphs and their between-group differences were calculated. This permutation test randomization procedure was repeated 1,000 times at each threshold, consistent with the real networks. Finally, the 95th percentile points of each distribution were used as the critical values for a one-tailed test of the null hypothesis with a probability of Type I error of 0.05. Moreover, we calculated the integrals of the efficiency metrics curves as the integrated metrics (I_{Eloc}, the integrated local efficiency; I_{Eglob}, the integrated global efficiency) over the preselected range of cost threshold. Between-group significances of three comparisons on the integrated metrics were also estimated by 1,000 permutation tests. For the investigation of node betweenness, we also computed the between-group significance of two comparisons (Y vs. M and M vs. O) on the integrated normalized betweenness (I_{BCi}) over the cost threshold range, using 1,000 permutation tests. To adjust for the multiple comparisons, a false discovery rate (FDR) procedure was applied at a q value of 0.05 [Genovese et al., 2002]. We also calculated the ratio of intermodule connections under a cost threshold range (0.11 ≤ cost ≤0.25, step = 0.01) with the modular organization by the cost of 0.11. An ANOVA analysis was applied to test the between-group significance of the ratio of intermodule connections.

RESULTS

Economical Small-World Properties and Age-Related Changes

We used a range for cost threshold (0.11 ≤ cost ≤0.25, step = 0.01) to verify the properties of structural brain networks from three age-specific groups (Young, 18–40 years; Middle, 41–60 years; Old, 61–80 years). With the cost thresholding strategy, both the local and global efficiency curves of structural brain networks in three groups were intermediate compared with those of the matched random and regular networks (Fig. 1A,B). The structural brain networks in three age-specific groups exhibited economical small-world properties, indicated by higher local and global efficiency than comparable random and regular networks, respectively [Latora and Marchiori, 2001].

As shown in Figure 1A, the local efficiency in the young group was significantly larger than those of the middle and old groups, whereas no significant difference was found between the middle and old groups. The global efficiency of the young group was significantly lower than that of the middle and old groups, and the old group had significant lower values than the middle group (Fig. 1B). Using the integrated efficiency metrics over the small-world regime, we defined a U-curve model to clarify the trend of topological properties of structural brain networks with normal aging. The integrated local and global efficiency showed a U-curve and an inverted-U-curve, respectively (Fig. 1C,D).

Regional Nodal Characteristics and Age-Related Changes

To identify the global hubs in structural brain networks, we averaged the normalized node betweenness centrality BC_i of each region over the cost threshold regime. The regions with higher $\overline{BC_i}$ (> mean + sd) were identified as the global hubs (Table III). In the young group, 16 regions were designated as the global hubs, specifically 14 association regions and 2 limbic/paralimbic regions. In the middle group, 14 regions were identified as the global hubs, specifically 10 association regions and 4 limbic/paralimbic regions. In the old group, 14 regions were identified as the global hubs, specifically 10 association regions, 3 limbic/paralimbic regions and 1 subcortical region. Among the identified global hubs, 12 of 16 regions in the young group, 9 of 14 regions in the middle group, and 7 of 14 regions in the old group were frontal and parietal regions. Results also indicated that 10 out of all 14 global hubs in the middle group and 6 out of all 14 global hubs in the old group were also identified as the global hubs in the young group. To further clarify the alteration of regional

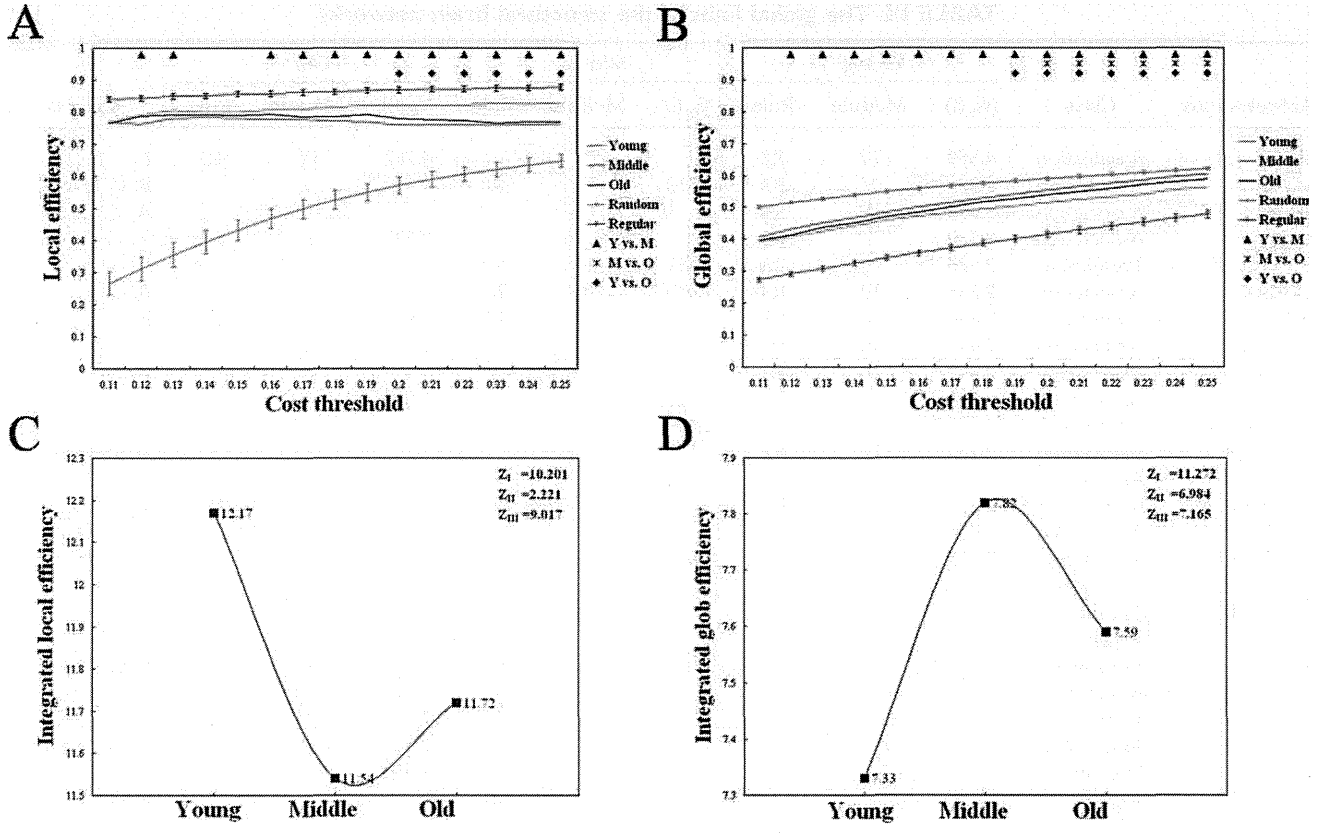

Figure 1.

Economical small-world properties and age-related changes. Left: The local and global efficiency of brain networks as a function of cost threshold. Right: The trend for the integrated efficiency metrics in age-specific groups. **A**: Local efficiency calculated under the cost threshold range of 0.11–0.25. **B**: Global efficiency calculated under the cost threshold range of 0.11–0.25. Significant differences between age groups were tested by permutation test under uncorrected conditions ($P < 0.05$). ▲; Y vs. M, ×; Y vs. M, ◆; Y vs. O. **C**: Integrated local efficiency. **D**: Integrated global efficiency. Three comparisons were performed as follows: Z_I (Young vs. Middle), Z_{II} (Middle vs. Old), and Z_{III} (Young vs. Old).

nodal characteristics, we applied 1,000 permutation tests to compute the significance of between-group differences in node betweenness ($P < 0.001$, FDR-corrected). The results indicated that six regions in the dorsal frontal-parietal junction [IFGoperc.L, SFGmed.L, SFGmed.R, SFGdor.L, IPL.L, PCUN.L; for abbreviation see Supporting Information Table SI] showed decreased node betweenness from young to middle age, whereas only three regions in the ventral frontal and temporal lobes [ORBinf.L, ORBinf.R, STG.L] revealed increased node betweenness (see Supporting Information Table SII). For the period from middle to old age, five ventral lateral cortices in the frontal and temporal lobes [ORBinf.L, ORBinf.R, ORBmed.R, MTG.L, MTG.R] showed decreased node betweenness, whereas nine regions mostly in the lateral occipital-parietal junction [MOG.L, MOG.R, ANG.L, ANG.R] and the paralimbic/subcortical area [PHG.R, AMYG.R, CAU.L, THA.L] revealed increased node betweenness (see Supporting Information Table SIII). The global hubs and the significant age-related changes in node betweenness were visualized by surface representations of structural brain networks using the Caret software [Van Essen, 2005], (see Fig. 2).

Modularity and Age-Related Changes

Maximum modularity (M) of brain networks decreased as a function of increasing cost threshold (see Supporting Information Fig. S1). It is generally accepted that $M \geq 0.3$ are indicative of nonrandom community structure [Newman and Girvan, 2004]. In this study, as the values of modularity were all larger than 0.3 over the preselected cost threshold range, and structural brain networks were consistently modularly organized in three age groups. However, there was no significant difference in modularity